# Sensing Gas Mixtures by Analyzing the Spatiotemporal Optical Responses of Liquid Crystals using 3D Convolutional Neural Networks

Nanqi Bao¹‡, Shengli Jiang²‡, Alexander Smith²‡, James J. Schauer³, Manos Mavrikakis², Reid C. Van Lehn², Victor M. Zavala²\* and Nicholas L. Abbott¹\*

KEYWORDS: liquid crystals, gas sensor, machine learning, spatiotemporal patterns, color features

ABSTRACT: We report how analysis of the spatial and temporal optical responses of liquid crystal (LC) films to targeted gases, when performed using a machine learning methodology, can advance the sensing of gas mixtures and provide important insights into the physical processes that underlie the sensor response. We develop the methodology using O<sub>3</sub> and Cl<sub>2</sub> mixtures (representative of an important class of analytes) and LCs supported on metal perchlorate-decorated surfaces as a model system. Whereas O<sub>3</sub> and Cl<sub>2</sub> both diffuse through LC films and undergo redox reactions with the supporting metal perchlorate surfaces to generate similar initial and final optical states of the LCs, we show that a 3-dimensional convolutional neural network (3D CNN) can extract feature information that is encoded in the spatiotemporal color patterns of the LCs to detect the presence of both O<sub>3</sub> and Cl<sub>2</sub> species in mixtures as well as to quantify their concentrations. Our analysis reveals that O<sub>3</sub> detection is driven by the transition time over which the brightness of the LC changes, while Cl<sub>2</sub> detection is driven by color fluctuations that develop late in the optical response of the LC. We also show that we can detect the presence of Cl<sub>2</sub> even when the concentration of O<sub>3</sub> is orders of magnitude greater than the Cl<sub>2</sub> concentration. The proposed methodology is generalizable to a wide range of analytes, reactive surfaces and LCs, and has the potential to advance the design of portable LC monitoring devices (e.g., wearable devices) for analyzing gas mixtures using spatiotemporal color fluctuations.

The development of new materials and methodologies for the sensing of targeted chemical species has the potential to be broadly useful in a range of contexts, including occupational health, 1,2 homeland security (toxic industrial chemicals), 3,4 or medicine (e.g., analysis of the breath).<sup>5</sup> In particular, there remains an unmet need for wearable sensors for human exposure measurements and health monitoring, <sup>6,7</sup> and light weight sensors for autonomous aerial vehicles. <sup>8,9</sup> Additionally, although metal oxide<sup>10-13</sup> and electrochemical amperometric <sup>14-16</sup> sensors possess limits of detection that make them potentially suitable for environmental monitoring, they are not approved for regulatory compliance testing by US regulatory agencies (the Environmental Protection Agency and the Occupational Safety and Health Administration) because they are not sufficiently stable or reliable. Liquid crystals (LCs), which combine key properties of crystalline solids (long-range order) and isotropic liquids (molecular mobility), are a promising class of chemoresponsive materials for designing wearable/portable sensors (e.g., badges for monitoring of exposure to toxic gases<sup>17</sup> and assays read out using a smartphone<sup>18</sup>). In this paper, we provide a methodological advance towards the development of sensors based on LCs that have attributes that may enable them to address the abovedescribed unmet needs.

LC-based sensors have been designed by exploiting changes in the mesoscale organization of bulk LC phases (e.g., cholesteric LCs and chemically sensitive chiral dopants) that are induced by targeted chemical species. 19-25 Alternatively, the LC sensor design investigated in this work relies on the use of reactive surfaces to trigger surface anchoring transitions of LCs.<sup>26-35</sup> Whereas the majority of past studies have analyzed the average intensity of light passing through LC-based sensors, here, we make an advance in methodology that involves analyzing the spatiotemporal optical responses of LCs to mixtures. By using machine-learning methods, we show that information embedded in the spatiotemporal optical response of the LC can be used to identify targeted gas species within a mixture and to quantify their concentrations. Additionally, we show that it is possible to use machine learning to provide physical insights into the processes that permit identification of targeted species from a given optical response of the LC sensor. We use Cl2 and O<sub>3</sub> as model chemical species to illustrate this methodology, but the approach is broadly applicable to wide range of analytes as well as potentially other classes of optical sensors.<sup>36</sup> The capability to analyze mixtures of Cl<sub>2</sub> and O<sub>3</sub> is relevant to applications such as air quality monitoring in urban environments and wastewater treatment facilities, where Cl<sub>2</sub> and O<sub>3</sub> are both used.37,38

<sup>&</sup>lt;sup>1</sup>Smith School of Chemical and Biomolecular Engineering, Cornell University, Ithaca, NY 14853, USA

<sup>&</sup>lt;sup>2</sup>Department of Chemical and Biological Engineering, University of Wisconsin-Madison, Madison, WI 53706, USA

<sup>&</sup>lt;sup>3</sup>Department of Civil and Environmental Engineering, University of Wisconsin-Madison, Madison, WI 53706, USA

<sup>\*</sup>Corresponding Authors

<sup>\*</sup>victor.zavala@wisc.edu

<sup>\*</sup>nla34@cornell.edu

Past studies have used machine-learning methods to analyze LC optical responses to single component gases but not mixtures. For example, so-called 2-dimensional convolutional neural networks (2D CNNs), which analyze the spatial patterns generated by LC responses (x, y, independent of time), have been used to extract information from LC responses to single component gas streams.<sup>39,40</sup> Alternatively, an ensemble of both 3D-CNNs (which analyze time-dependent spatial patterns (t, x, y)) and 2D-CNNs with Long Short-Term Memory networks (a class of CNNs that is well-suited to measurements of time series data) has also been reported for analysis of the dynamic optical response of LC droplets to exposure to individual VOCs (single-component gas streams). 41 However, a disadvantage of ensemble methods is that they prevent interpretation of the output of the CNN in terms of physical mechanisms. Whereas these prior studies focus on single component streams, a key contribution contained in the work reported in this paper is the design a 3D CNN (that we call LCNet) that extract features from highly complex spatio-temporal color patterns that develop during the LC system response to O<sub>3</sub>/Cl<sub>2</sub> mixtures. Although these features are straightforward to identify in the LC response to single gaseous species, the experiments reported in this paper reveal that without use of CNNs, these space-time features are difficult to quantify and detect in complex gaseous mixtures.

The LCNet architecture reported herein provides a framework to analyze large amounts of video data that were generated by performing high-throughput experiments with LCs. In LCNet, a video capturing the LC response is represented as a multi-channel 3D tensor (multi-dimensional array, see details in Methods and Supporting Information (SI)) in which every channel is a 3D tensor that contains the space-time response of a color channel. As such, the 3D CNN can simultaneously extract features from space-time patterns for red (R), green (G), and blue (B) channels and can capture dependencies between such channels. The data representation used by the 3D CNN is comprehensive and prevents loss of key information that is encoded in spatial, temporal, or color patterns. The feature information extracted by the 3D CNN can be used in a wide variety of tasks relevant to sensor performance such as classification (for detecting the presence of a particular chemical species) and

regression (for quantifying the concentrations of single or multiple chemical targets). Specifically, we show that LCNet can predict the presence of  $O_3$  (accuracy of  $99 \pm 1\%$ ) and  $Cl_2$  (accuracy of  $93 \pm 3\%$ ) in a gaseous mixture, where accuracy is defined as = (number of samples in which an analyte is present is classified as having an analyte present (true positive) + number of samples in which an analyte is absent is classified as having no analyte present (true negative)) / total number of samples × 100%. Notably, we show that such accuracies can be obtained for gaseous environments that are dominated by O<sub>3</sub> (with concentrations that are three orders of magnitude higher than those of Cl<sub>2</sub>). This indicates that LCNet can effectively identify subtle signatures that are present in the LC responses. Moreover, we show that LCNet can predict the concentration of O<sub>3</sub> and Cl<sub>2</sub> in a mixture and that it generalizes to concentrations not included in the training procedure.

We have also equipped LCNet with so-called saliency analysis techniques that identify the spatial and temporal characteristics of the LC response that contain information about the mixture composition. This analysis allows us to gain key insights that can inform the design of LC systems and that can help us understand physical phenomena underlying the LC response (see SI for more details on saliency analysis).<sup>42</sup> Specifically, we use saliency analysis to reveal specific features of the optical response that are critical in detecting O<sub>3</sub> and Cl<sub>2</sub> in mixtures. For instance, we find that the response time of brightness is the critical feature that enables O<sub>3</sub> sensing, while space-time color dynamics is the critical feature that enables Cl<sub>2</sub> sensing. Additionally, our results reveal that the presence of Cl<sub>2</sub> in a mixture (even at low concentrations) influences the response dynamics, and that color fluctuations triggered by Cl<sub>2</sub> persist even after brightness has saturated. This result indicates that Cl<sub>2</sub> cannot be easily detected in mixtures using optical response features that ignore color. Our analysis also reveals that the A\* channel in the L\*A\*B color space provides an informative descriptor that facilitates the analysis of color dynamics and thus quantification of Cl<sub>2</sub> concentration in mixtures. These results demonstrate that machine learning provides new approaches to the design of LC-based sensors that can analyze complex mixtures.

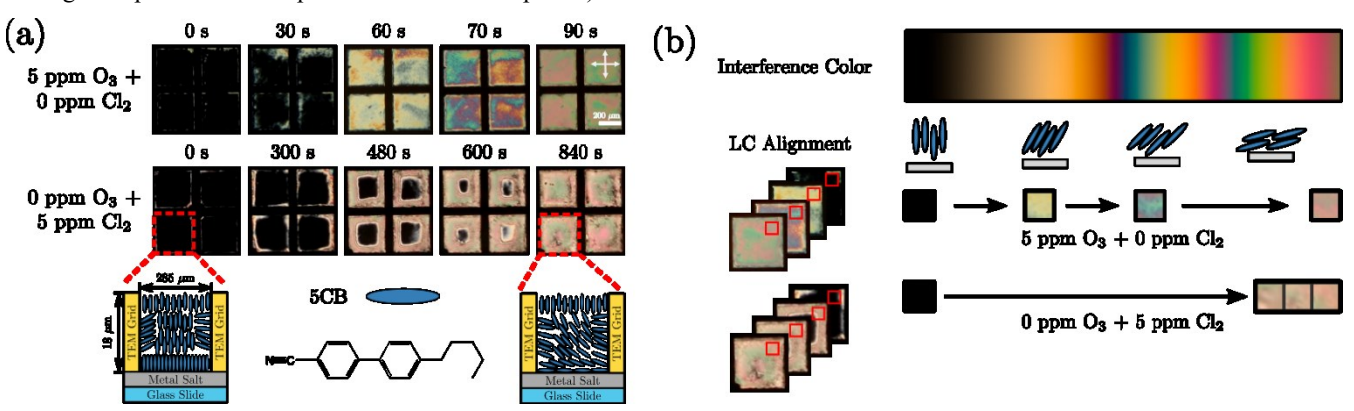


Figure 1. (a) Optical micrographs (top view, crossed polarizers) of 5CB hosted in copper grids (lateral size of each grid square is 285 μm) on surfaces decorated with 15±3 pmol/mm² Mn(ClO<sub>4</sub>)<sub>2</sub> recorded 0, 30, 60, 70 and 90 seconds after initial exposure to 5±1 ppm O<sub>3</sub> gas at 20% RH, or 0, 300, 480, 600 and 840 seconds after initial exposure to 5±0.2 ppm Cl<sub>2</sub> gas at 20% RH. Below the optical images is a representation (side view) of the homeotropic (perpendicular) orientation of 5CB hosted in a copper grid before gas exposure (initial state), and the planar (parallel) orientation of 5CB after gas exposure (final state). Blue ellipses represent 5CB molecules (the mesogen). (b) Visualization of interference colors created by white light illumination when liquid crystals transition from homeotropic to planar orientation (interference colors are a result of liquid crystal birefringence and tilt angle). Pure O<sub>3</sub> triggers a *continuous* anchoring transition, resulting in a "jump" in interference colors.

#### EXPERIMENTAL MATERIALS AND METHODS

Materials. Manganese (II) perchlorate hydrate and potassium iodide were purchased from Sigma-Aldrich (Milwaukee, WI). Fischer's Finest glass slides and starch indicator 1% for iodometric titration were purchased from Fischer Scientific (Pittsburgh, PA). Absolute ethanol (anhydrous, 200 proof) was purchased from Pharmco-AAPER (Brookfield, CT). All chemicals and solvents were of analytical reagent grade and were used as received. Deionized water possessed a resistivity of at least 18.2 MΩ cm or greater. 5CB was purchased from Jiangsu Hecheng Advanced Materials Co., Ltd (Jiangsu, China). Cl2 in nitrogen gas (purity of Cl2 is 99.9% and purity of nitrogen is 99.998%) at a concentration of 10 ppm and nitrogen gas (99.998% purity) were obtained from Airgas (Elmira, NY) and used as received. Ozone gas was generated from an ozone generator (A2Z Ozone Inc., Louisville, KY). Sodium thiosulfate was purchased from MilliporeSigma (Burlington, MA) for iodometric titration.

Formation of LC films supported on functionalized surfaces. Glass slides were rinsed with copious amounts of ethanol and then dried under a stream of nitrogen. Metal ions were deposited onto the glass surfaces by spin coating ethanolic solutions of 1.5 mM Mn(ClO<sub>4</sub>)<sub>2</sub> at 3000 rpm for 30s (WS-400A-6NPP/Lite, Laurell Technologies, North Wales, PA). The Mn cation surface density was measured to be 15.2±2.6 pmol/mm<sup>2</sup>, as determined by using inductively coupled plasma optical emission spectrometry (ICP-OES, Perkin Elmer 4300)<sup>34</sup>. After coating the surface with the metal salt, an 18 µm-thick copper transmission electron microscopy (TEM) grid (Electron Microscopy Sciences, Hatfield, PA) was placed on the metal-salt surface. The TEM grid had an overall diameter of 3 mm and was composed of square pores with lateral dimensions of 285 μm. The grids were filled with 0.1 μL of nematic 5CB using a microcapillary. The excess LC was removed from the grids by wicking the LC into an empty microcapillary tube.

Generation of gases. O<sub>3</sub> concentration within the gas stream fed to the LC was controlled by changing the ratio of N2 and O2 in the gas input to an ozone generator; a schematic illustration is shown in the SI (Figure S1). A higher concentration of O2 fed to the O3 generator produced a higher concentration of O<sub>3</sub> gas (up to a few hundred ppm) as determined by using iodometric titration. Detailed descriptions of iodometric titration can be found in prior publications 43,44. The diluted O<sub>3</sub> concentration was measured by using an O<sub>3</sub> detector tube (Sensidyne, St. Petersburg, FL). The stream of gas containing Cl<sub>2</sub> was sourced from a certified cylinder containing 10 ppm Cl<sub>2</sub> in nitrogen and diluted with N2 to the desired concentrations. The specific relative humidity of the gas stream fed to the LC was controlled at 20% RH by passage of the gas through a portable dew point generator (LI-610, LI-COR Biosciences, Lincoln, NE).

Exposure of LC films to gaseous mixtures containing O<sub>3</sub> and Cl<sub>2</sub>. LC samples hosted within the TEM grids supported on the Mn(ClO<sub>4</sub>)<sub>2</sub>-decorated surfaces were exposed to a stream of Cl<sub>2</sub> or/and O<sub>3</sub> within a flow cell that was constructed to direct the gaseous flow across the LC samples while permitting observation of the samples through a polarized-light microscope (CH40, Olympus, Melville, NY) (Figure 1a). A detailed description of the flow cell can be found in a prior publication<sup>45</sup>. White light illumination was used in the microscopic observations (Philips 6V 30W G4 halogen bulb; Philips, Cambridge, MA) and videos of the optical responses (crossed-polars, transmission mode) of the LCs were recorded using a Canon T6i camera (Canon U.S.A. Inc., Huntington, NY). The videos were

recorded at ISO 400 and 1/30 shutter speed (29.97 frames/second) with a resolution of 1920x1080. The gas fed to the flow cell was maintained at room temperature (approximately 23°C). The flow rate of each gas stream was controlled using a series of rotameters (Aalborg Instruments and Control, Orangeburg, NY). The total flow rate was maintained at 1200 mL/min at atmospheric pressure. For gas mixtures, Cl<sub>2</sub> and O<sub>3</sub> gases with designed concentrations were mixed before being delivered to the flow cell. We explored gas mixtures containing four  $O_3$  concentrations (650±20, 100±10, 5±1, and 1.5±0.2 ppm) and three Cl<sub>2</sub> concentrations (5 $\pm$ 0.2, 2 $\pm$ 0.08, and 1 $\pm$ 0.04 ppm) (see SI for additional details). These concentrations were selected for two reasons. First, these gas compositions generated LC responses that were indistinguishable to the eye (Figure 1b). Second, these gas compositions generated LC responses that were not measurably different when quantified using previous metrics of LC response such as the average intensity of transmitted light (see discussion below in the context of Figure 4). In addition, we also deliberately explored mixtures containing a swamping concentration of one species (O<sub>3</sub>) to challenge the ability of LCNet to quantify mixtures under more demanding conditions. However, the effect of no exposure data is discussed in the SI. In total, we explored sixteen concentrations with at least three videos per condition. In each video, we recorded the anchoring transitions of LCs that were confined within 32 square grids (each with dimensions of 285 µm x 285

### COMPUTATIONAL METHODS

**Data Preparation.** Video data of the LC-filled TEM grids were used to analyze LC responses to different gaseous environments (Figure 1). The responses of the LC systems are represented as multi-channel 3D tensors (Figure 2), which is the data representation required by 3D CNNs. To obtain this representation, we split the TEM grid into 12 square grids, as shown in Figure 2 and in the SI (Figure S3 and S4). Each grid square is defined as a chemoresponsive LC system; for each square, we capture an image (48x48) every 1 sec and stack them chronologically into a tensor. The tensor of each square thus has three dimensions, corresponding to space (directions (x, y) and time (t). The response times of the LC systems under different gaseous environments were found to differ significantly (as detailed below in text accompanying Figure 4). To obtain a consistent data representation, each video was cropped to obtain a total of t=120 seconds because the LC responded to all mixture concentrations within t=100 seconds (as detailed below in Figure 4). As such, each grid square generates a 3D tensor of dimension 48x48x120. Another important aspect of the response data collected is that it is recorded in RGB format; as such, each image contains three channels (intensity fields for red, green, and blue). Each grid square thus generates a 3-channel, 3D tensor. This data representation is complex but comprehensive because it simultaneously captures space, time, and color information of the LC responses. It is important to highlight that the response of each grid square contains a significant amount of data; specifically, each 3-channel, 3D tensor contains 829,440 data entries. We will refer to each entry as a voxel, which represents a point in space-time. A voxel is a 3D generalization of a pixel (a point in a 2D space). The dataset studied contains a total of 948 LC system responses (with 96 to 384 responses (augmented grid videos) for every gaseous mixture concentration, see details in Table S1). Each of these responses generates a dataset that is input to the LCNet and is paired with two real-valued scalar outputs (labels), denoted  $C_{O3}$  and  $C_{Cl2}$  (which represent the concentration of  $O_3$  and  $Cl_2$  in the gaseous environment).

## 3D Convolution Neural Network Architecture (LCNet).

The main hypothesis driving our work is that space-time responses of LC systems encode significant information that enables the detection of O<sub>3</sub> and Cl<sub>2</sub> in gaseous mixtures and the prediction of their concentrations. Methods previously reported in the literature characterize these responses by using descriptors that might fail to capture important information. For instance, the response time of the brightness (spatially-averaged) has been used to detect and measure analyte concentration<sup>32,46,47</sup>. In this work, we develop a 3D CNN that we call LCNet; this ML architecture aims to systematically capture spatial, temporal, and color features of LC responses.

LCNet is implemented in TensorFlow<sup>48</sup>; a detailed explanation of the inner mechanics and the full architecture is presented in the SI (Section S3). A simplified representation of the operations performed in LCNet is shown in Figure 2; here, we illustrate the creation of the tensor representation via stacking of snapshots for each TEM square. LCNet uses two primary computational operations, which are known as *convolution operations* (filtrations) and max-pooling. Convolution operations are the primary operation for extracting informative patterns/signatures or morphologies from a given input in a 3D CNN. In LCNet, each filter is a tensor of dimension 3x3x3; each of these filters applies a pattern matching operation on a 3x3x3 neighborhood of each voxel. The filters are parameters that can be learned to extract patterns that best match data. The convolution of a filter with a voxel returns a single scalar value,

which signifies the presence (high value) or absence (low value) of the pattern that the filter is seeking to identify. In our architecture, we refer to a set of these convolution operations as the *convolutional layer*. A convolution operation over a tensor will map the tensor into a filtered tensor of the same dimension; thus, a tensor that is passed through a convolutional layer is mapped to multiple transformed tensors (one for each filter). The convolution layer thus increases the amount of data processed exponentially; as such, max-pooling layers are used to reduce the dimension of the filtered tensors. In LCNet, the max-pooling operation takes a 2x2x3 section of a filtered tensor (containing 12 entries) and summarizes it into a single value (the maximum value). This reduces the dimension of the tensors created and distills important information extracted by the filters. In LCNet, convolutional layers and max-pooling layers are performed recursively. This recursion seeks to extract information at multiple space-time scales (local and global). while summarizing information. The information extracted by the convolutional layers is summarized in a stacked vector that is fed to a fully-connected neural network. This network propagates the feature information obtained from the convolution and max-pooling layers through a sequence of perceptron layers. The parameters of these layers (weights and biases) are adjusted to match the model predictions to the experimental labels (analyte type of concentrations). The fully-connected neural network can thus perform classification tasks (analyte detection) or regression tasks (prediction of analyte concentration) based on feature information extracted from convolutional and pooling layers.

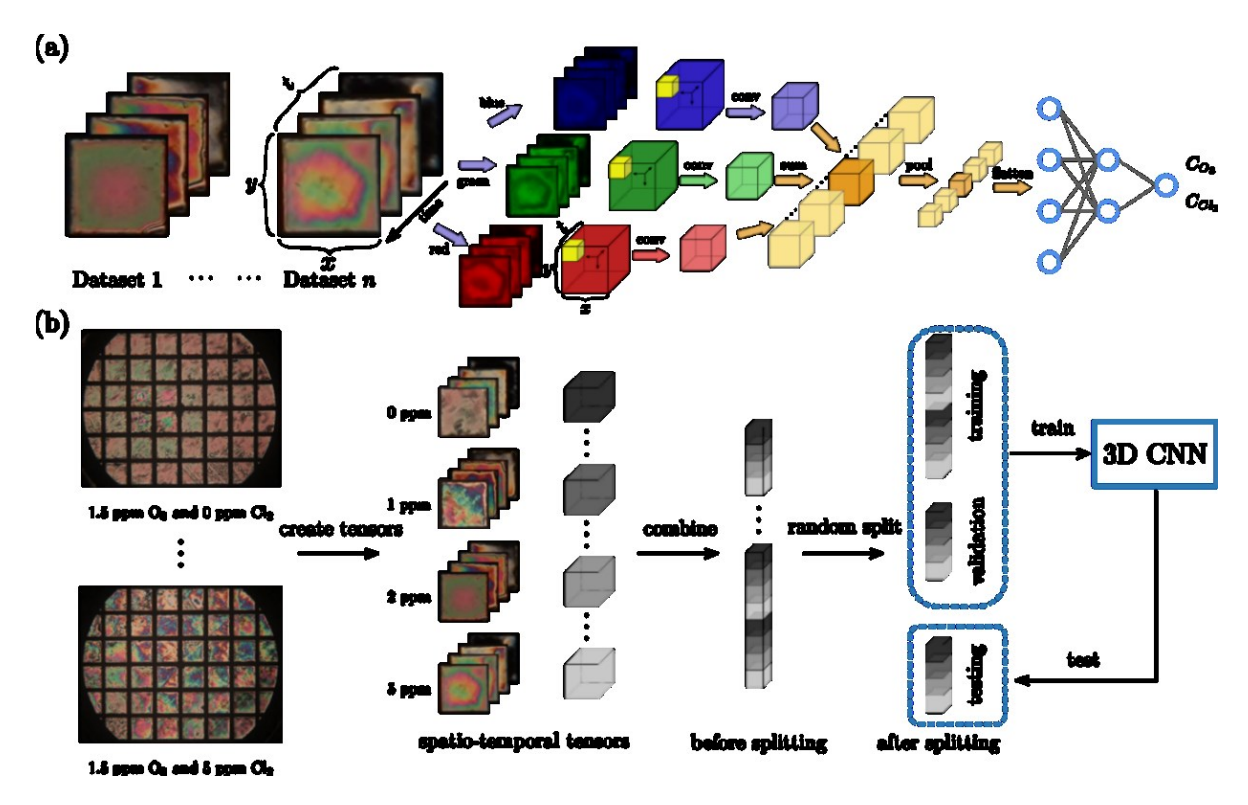


**Figure 2.** (a) Schematic of machine learning workflow for data pre-processing, training, and prediction. The video data of each grid square divided into 1-sec snapshots that are stacked into a 3D tensor containing three channels (*red*, *green*, and *blue*). This 3-channel, 3D tensor is processed via convolutional filters and max pooling operations to extract information. The feature information obtained from convolution and pooling is flattened into a single vector and then is fed into a fully-connected layer that detects Cl<sub>2</sub> and O<sub>3</sub> (classification) or predicts their concentrations (regression). (b) Schematic diagram of training, validation, and testing procedures utilized to provide a statistically valid estimate of the performance of the 3D CNN. The entire dataset is split into independent sets of testing, validation, and training videos. The training and validation videos are used to optimize the parameters of the 3D CNN model. Predictions are then made on the testing videos in order to estimate the accuracy of the model.

LCNet Training and Testing. A primary factor that determines the effectiveness of a 3D CNN is the training and corresponding testing of the trained network (Figure 2). We note that the datasets for exposure of LCs to a single gas are part of the overall dataset. For example, as shown in Figure 2b, the data for single gas exposure to O<sub>3</sub> (when the concentration of Cl<sub>2</sub> is zero; 1.5 ppm  $O_3$  and 0 ppm  $Cl_2$ ) is part of the overall dataset. The total dataset is randomly split into a training set, validation set, and testing set. While the architecture of LCNet is predetermined (e.g., number of filters, number of layers, size of filters), the parameter values associated with the convolutional layers (filters and biases) and fully-connected layers (weights and biases) need to be learned from data via training and validation. The training and validation of LCNet provide the network with a set of input tensors, taken from the training set, and their corresponding output labels. The 3D CNN will then attempt to predict the label from the input data and will compare this prediction to the true experimental value of the output label. For presence classification, the label is the presence of O<sub>3</sub> or Cl<sub>2</sub>. For concentration regression, the label contains the O<sub>3</sub> and Cl2 concentrations. We also implemented a sequential classification approach to determine the limit of detection of the concentration of O<sub>3</sub> and Cl<sub>2</sub> in the mixture. In the first step, we performed concentration classification for O<sub>3</sub> for the range of concentrations (0, 1.5, 5, 100 and 650 ppm) using the entire dataset. In the second step, we classified the concentration of Cl<sub>2</sub> (0, 1, 2 and 5 ppm) using the O<sub>3</sub> concentration classified in the first step. In this approach, the training label is the level of O<sub>3</sub> or Cl<sub>2</sub> concentration. The difference between the predicted values and the experimental values is known as the *error*. The 3D CNN will then adjust its parameters (by minimizing a loss/error function) to reduce the magnitude of the error. This is done multiple times for every training input in order to minimize the total error for all the training inputs. Along with the training set, the validation set is used to prevent overfitting of the trained model. The validation set acts as a preliminary testing set, allowing the model to be evaluated on the data it is being trained on as well as on a separate dataset that helps identify the optimal model parameters. Once the network has been trained, its generalizability is probed against a testing set. In order to further improve the generalizability of the LCNet, we perform a task known as k-fold cross-testing. 49 The data is split into k subsets where k-l subsets are used for training/validation and I subset is used for testing. The training/validation and testing are performed k times; each time a different subset is used for testing and all other subsets are used for training/validation. In our framework we use k=5; this gives a simple resampling procedure that provides robust performance.50

#### RESULTS AND DISCUSSION

Responses of LC films to gaseous mixtures containing O<sub>3</sub> and Cl<sub>2</sub>. We performed experimental measurements of the optical response of LCs to mixtures of Cl<sub>2</sub> and O<sub>3</sub> using nematic 5CB films supported on Mn(ClO<sub>4</sub>)<sub>2</sub>-decorated surfaces. This choice of experimental system was guided by prior studies (as shown in Figure 1) that demonstrated that 5CB responds to either Cl<sub>2</sub> or O<sub>3</sub> on these surfaces because both gases diffuse through the LC to oxidize Mn<sup>2+</sup> (in the form of Mn(ClO<sub>4</sub>)<sub>2</sub>) to Mn<sup>4+</sup> (in the form of MnO<sub>2</sub>), a result confirmed by using Raman spectroscopy<sup>51</sup> or powder X-ray diffraction.<sup>52</sup> The formation of the MnO<sub>2</sub> on the surface weakens the binding of the 5CB molecules, thus resulting in an LC orientational transition (Figure 1). The anchoring transition of the LC that is induced by the surface reaction can be easily visualized by using optical methods (e.g., by viewing the LC film using white light in

transmission mode between cross polarizers). Due to the birefringence of LCs, changes in color and brightness are observed to accompany orientational transitions. This sensor design principle is illustrated on the left side of Figure 1a; when the LCs exhibit homeotropic alignment, light is unable to pass through crossed polarizers (transmissions mode) and the micrograph of the LC film appears black. After exposure to a gaseous analyte, the LCs reorient and alter the polarization of light traveling through the film, resulting in complex space-time color response patterns. The formation of the MnO2 is irreversible, which generates an irreversible LC optical response, making this system potentially suitable for use in sensors that alarm upon exposure to a threshold concentration of gas or provide measurements of cumulative exposure to a gas (e.g., dosimeters). <sup>53</sup>

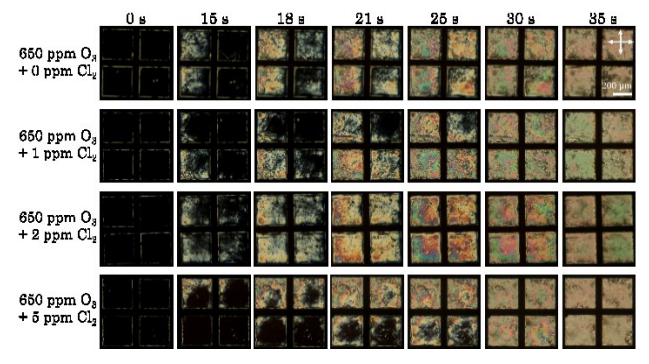


**Figure 3.** Optical micrographs (top view, crossed polarizers) of 5CB on surfaces decorated with 15±3 pmol/mm<sup>2</sup> Mn(ClO<sub>4</sub>)<sub>2</sub> recorded 0, 15, 18, 21, 25, 30 and 35 seconds after initial exposure to the gas mixtures of 650±20 ppm O<sub>3</sub> with 0, 1±0.04, 2±0.08 and 5±0.2 ppm Cl<sub>2</sub> at 20% RH.

To examine the responses of LC to mixtures of O<sub>3</sub> and Cl<sub>2</sub>, we exposed 5CB on surfaces decorated with 15±3 pmol/mm<sup>2</sup> Mn(ClO<sub>4</sub>)<sub>2</sub> to O<sub>3</sub>-Cl<sub>2</sub> mixtures with 16 distinct compositions. The gas mixtures contained four O<sub>3</sub> concentrations (650±20,  $100\pm10$ ,  $5\pm1$ , and  $1.5\pm0.2$  ppm), and three Cl<sub>2</sub> concentrations  $(5\pm0.2, 2\pm0.08, 1\pm0.04, and 0 ppm)$ . Representative optical responses to mixtures of 650±20 ppm O<sub>3</sub> and varying Cl<sub>2</sub> concentrations (0,  $1\pm0.04$ ,  $2\pm0.08$  and  $5\pm0.2$  ppm) at 20% RH are presented in Figure 3. Inspection of Figure 3 reveals that all LC responses share a common set of characteristics; specifically, the optical response starts at 15 seconds and is complete after 35 seconds, and changes in LC interference colors accompany the exposures (consistent with a continuous LC anchoring transition). We also observe that the dynamic response of the LC to the gas mixtures containing 650±20 ppm O<sub>3</sub> and various concentrations of Cl2 does not obviously vary with Cl2 concentration. This result indicates that the optical response of the LC is dominated by O<sub>3</sub> (Figure 3). This observation holds true for other mixture compositions (100 $\pm$ 10, 5 $\pm$ 1, and 1.5 $\pm$ 0.2 ppm O<sub>3</sub> with  $5\pm0.2$ ,  $2\pm0.08$ , and  $1\pm0.04$  ppm Cl<sub>2</sub>), as seen in Figure 4. Inspection of Figure 4 also reveals significant variability in the dynamics of the LC optical responses, particularly at low O<sub>3</sub> concentrations. This result indicates that temporal features will likely not provide robust detection and prediction of O<sub>3</sub> concentrations. Additionally, in Figure 3, we observe significant variability in the spatial response patterns (for different grid squares), indicating that it would be difficult to determine gas concentrations from snapshots of the LC (which ignore temporal information).

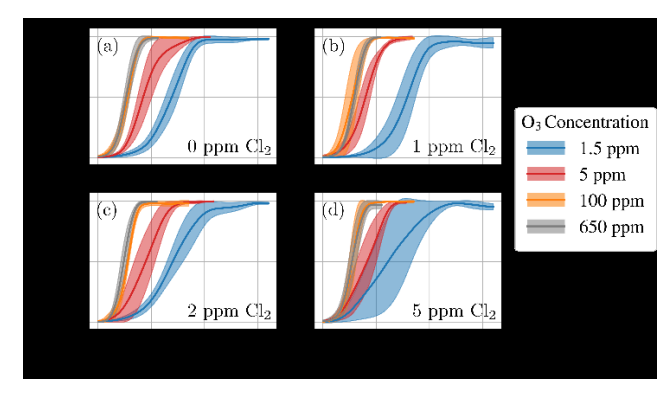


**Figure 4.** Normalized intensity of polarized light transmitted through 5CB supported on surfaces decorated with  $15.2\pm2.6$  pmol/mm² Mn(ClO<sub>4</sub>)2 exposed to the mixtures of O<sub>3</sub> at  $650\pm20$ ,  $100\pm10$ ,  $5\pm1$  and  $1.5\pm0.2$  ppm and Cl<sub>2</sub> at (a) 0, (b)  $1\pm0.04$ , (c)  $2\pm0.08$ , and (d)  $5\pm0.2$  ppm. The shaded area represents the standard deviation of the intensity at a given time. The response time varies with O<sub>3</sub> concentration, demonstrating that higher concentrations of O<sub>3</sub> result in faster response times. However, when the Cl<sub>2</sub> concentration is varied there is no perceptible difference in the dynamic characteristics of the responses. This suggests that temporal features can be used to detect and predict O<sub>3</sub> but not Cl<sub>2</sub>.

**Detection and Concentration Prediction.** After training, we used LCNet to predict the concentrations of Cl<sub>2</sub> and O<sub>3</sub> in gas mixtures of the types described in Figure 3 and 4. The results for concentration predictions (regression) of ~300 test samples using LCNet are shown in Figure 5 a and b. Inspection of Figure 5a reveals that LCNet can predict O3 concentrations with high accuracy, confirming that O3 triggers LC responses that contain significant information.<sup>52</sup> These results also show that the accuracy of the prediction is not affected by Cl2 concentration. The predictions for Cl<sub>2</sub> (Figure 5b) reveal that LCNet can also distinguish Cl<sub>2</sub> concentrations (even in the presence of high concentrations of O<sub>3</sub>). However, it is also evident that accuracy is not as high as that obtained for O3; this indicates that Cl<sub>2</sub> triggers optical responses in the LC that are less informative. This conclusion is confirmed by species identification results (classification; Figure 5c and d). Specifically, we found that LCNet provides a true-positive accuracy of 97% for Cl<sub>2</sub>, but has a 76% true-negative rate, equal to a false-negative rate of 24% (Figure 5d). The results highlight that it is difficult to detect Cl2 from optical responses of LCs to gas mixtures.

From the regression plot for the prediction of O<sub>3</sub> or Cl<sub>2</sub> concentration in Figure 5a or b, we found that 100 ppm O<sub>3</sub> or 2 ppm Cl<sub>2</sub> cannot be reliably distinguished from 0 ppm. To improve the limit of detection of O<sub>3</sub> and Cl<sub>2</sub> in the mixtures, we used a sequential classification approach. In the first step, we classified the O<sub>3</sub> concentration (for the range of concentrations of 0, 1.5, 5, 100 and 650 ppm) using the entire dataset; in the second step, we classified the concentration of Cl<sub>2</sub> (0, 1, 2 and 5 ppm) using the O<sub>3</sub> concentration classified in the first step. Inspection of Figure 5e reveals that we can discriminate each O<sub>3</sub> concentration with an overall accuracy of 99% and significantly, we can discriminate between the  $1.5\ ppm$  and 0ppm O<sub>3</sub> concentration classes with 99% accuracy. Inspection of Figure 5f reveals that we achieve an overall classification accuracy of 83% for Cl<sub>2</sub> concentration. In particular, we can discriminate between 1 ppm and 0 ppm Cl<sub>2</sub> concentration classes with an accuracy of 81%.

We also tested the generalizability of LCNet by predicting concentrations for a gaseous mixture containing 3.5 ppm  $\text{Cl}_2$ 

and 650 ppm  $O_3$ . Response data for LC systems at this mixture composition was not used in the training/validation of LCNet and this experiment was designed to simulate performance in an environment that is completely unknown (within the calibrated detection range of the sensor; 0-5 ppm  $Cl_2$ ). From Figure 5a and 5b, we see that LCNet predicts a concentration of  $3.59 \pm 1.35$  ppm  $Cl_2$  and a concentration of  $587 \pm 122$  ppm  $O_3$  (red), predictions that are in good agreement with the experimental conditions.

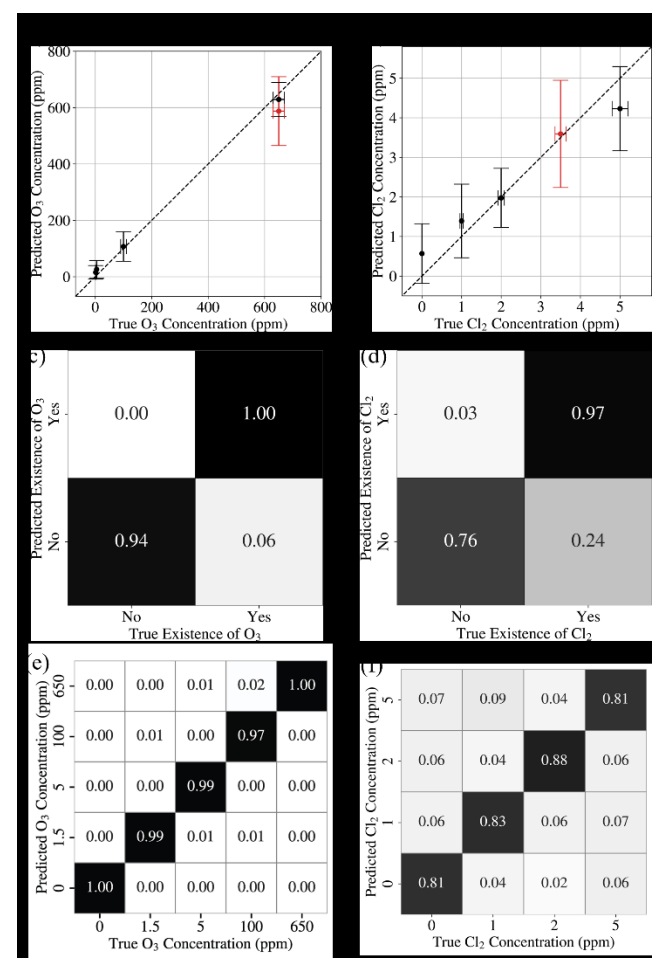


**Figure 5.** Regression plot for the prediction of (a) O<sub>3</sub> concentration or (b) Cl<sub>2</sub> concentration from LC response data using LCNet. The red data point indicates predicted O<sub>3</sub> or Cl<sub>2</sub> concentration of the never-before-seen sample with 650 ppm of O<sub>3</sub> and 3.5 ppm of Cl<sub>2</sub>. This data had been kept completely separate from the training set (to demonstrate the robustness of the predictions). Classification results (accuracy) for the presence of (c) O<sub>3</sub> or (d) Cl<sub>2</sub> in gaseous mixtures. Classification results (accuracy) for the concentration of (e) O<sub>3</sub> or (f) Cl<sub>2</sub> in gaseous mixtures. The diagonal entries are the fraction of LC responses correctly classified for the given concentration.

Reduced Data Representations. 3D CNNs do not permit easy identification of the key features (descriptors) that drive their predictions. Specifically, it is difficult to identify the signatures of the LC responses that are being used by the CNN to detect O<sub>3</sub> and/or Cl<sub>2</sub>. We addressed this issue by conducting a systematic analysis under different reduced data representations. Our data reduction procedure trained CNNs that ignore specific features of the LC responses (space, time, and color). Specifically, we eliminate spatial information by conducting spatial-averaging; we eliminate time information by analyzing a snapshot at the final time; and we eliminate color information by analyzing grayscale snapshots (average of RGB channels).

New CNNs were trained under these reduced data representations (1D and 2D CNNs) and their prediction performance was compared with that of LCNet (3D CNN which uses a complete data representation). A detailed explanation of the procedure and of the results can be found in the SI. In brief, we found that the information needed to accurately sense O<sub>3</sub> within the mixture with Cl<sub>2</sub> is minimal; temporal information can be used by a 1D CNN to obtain reasonable predictions (spatial and color information does not have a strong effect). Specifically, we observed a modest increase in the regression RMSE (relative to that of LCNet) when removing spatial information (+10%) but a large increase when removing temporal information (+143%; Figure S9). These results are in agreement with the results reported by Bao, et al., who correlated the response time of the LC to O<sub>3</sub> concentration (not in mixtures) using a simple linear regression model. 52 In the analysis of Cl<sub>2</sub> on the other hand, our data reduction analysis led us to conclude that removing spatial information results in a +54% increase in the RMSE and that removal of temporal information results in a +83% increase (Figure S9). This result confirms the need to simultaneously capture spatial and temporal information when detecting Cl<sub>2</sub>.

Saliency Analysis. We used saliency analyses to further investigate key features that enable LCNet to detect the presence of Cl<sub>2</sub> and O<sub>3</sub> within the mixtures. Saliency maps were used to identify voxels within an input tensor that have the largest influence on the final prediction of the 3D CNN<sup>42</sup>. A saliency map assigns a scalar value to each voxel that correlates with its influence on the final prediction (the saliency map is a 3D tensor). The saliency value at each voxel is determined by a perturbation of the given voxel and a subsequent prediction (i.e., via sensitivity analysis). Our goal was to identify which voxels in our spatio-temporal dataset have the greatest influence on the detection of a given chemical species (Cl<sub>2</sub> or O<sub>3</sub>) by the CNN. A detailed description of this process is found in the SI; here we provide a summary of the main findings using an illustrative example of saliency maps for a LC system exposed to a gaseous mixture (5 ppm O<sub>3</sub> and 2 ppm Cl<sub>2</sub>; Figure 6). In particular, we explore the spatial-average of the saliency map in order to identify key times in the response that influence the prediction. The saliency analysis in Figures 6a and 6b indicate that the key factor determining LCNets prediction of O<sub>3</sub> concentration is the response time; specifically, we can see that there is a peak in the saliency value at t = 33s, which is the time at which the LC optical response is first evident. We also observe a peak in the saliency value at t = 52s, which is the time at which the response brightness intensity saturates. The presence of the two peaks indicates that LCNet is using the transition time to characterize the O<sub>3</sub> concentrations. In contrast, inspection of Figures 6c and 6d reveals that the transition time is not used by the CNN for characterization of Cl<sub>2</sub> concentration. Specifically, we can see that saliency exhibits dynamics after the brightness has saturated (t = 52s) and the high values postsaturation indicate that these features are important in the detection of Cl<sub>2</sub>. These results indicate that the presence of Cl<sub>2</sub> in a mixture of Cl<sub>2</sub> and O<sub>3</sub> changes the final stage of the LC response and that this effect is detectable by the CNN.

Color Analysis. We determined that the saliency dynamics that develop late in the LC response to mixtures of Cl<sub>2</sub> and O<sub>3</sub> (after brightness has been saturated) are governed by fluctuations in color. This conclusion was reached by a transformation of the RGB channels of the input tensor into the L\*A\*B\* color space. The details of this transformation are explained in the SI. Our main goal in transforming RGB to L\*A\*B\* is to utilize the A\* channel, which represents a measure of intensity of red or green channels (negative values indicate green intensity and

positive values indicate red intensity). In other words,  $A^*$  is a descriptor that simultaneously captures information from red and green channels. Inspection of Figures 6c and 6d reveals that the complex spatio-temporal color patterns that characterize the LC response are described by changes in the value of  $A^*$ . Specifically, we noted that  $A^*$  exhibits dynamics after the brightness of the LC response has saturated. In Figure 6c, we present a time series of the spatial-average of  $A^*$ ; the spatial averaging reveals a strong correlation between the timing of the saliency and  $A^*$  peaks. This indicates that LCNet is exploiting dynamics of color patterns to detect the presence of  $Cl_2$  in mixtures.

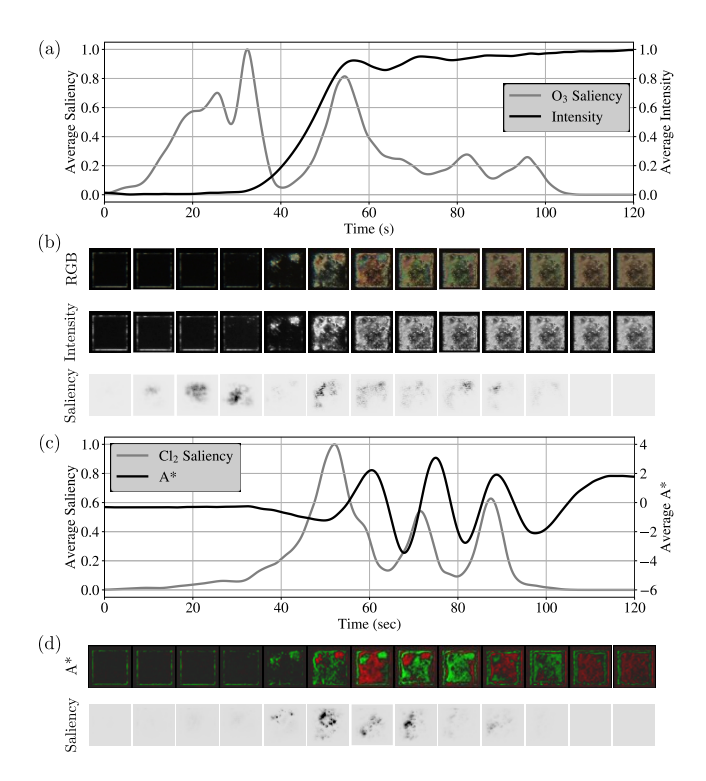


**Figure 6.** (a) Spatial-average of brightness intensity and saliency (for detection of O<sub>3</sub>) for a liquid crystal response to a mixture of 5ppm O<sub>3</sub> and 2ppm Cl<sub>2</sub>. (b) Snapshots of LC response at representative times shown in RGB and grayscale (intensity), along with the associated saliency maps. (c) Spatial-average of A\* and saliency corresponding to the same LC response and (d) A\* snapshots corresponding to saliency maps (for detection of Cl<sub>2</sub>). These results highlight that the spatio-temporal data representation used by the 3D CNN automatically identifies key signatures for the detection of O<sub>3</sub> (response time) and the driving factor for the detection of Cl<sub>2</sub> (color fluctuations near the end of the response). The saliency maps also have identified key color spaces (A\*) for the future study of the physics of liquid crystal sensor responses.

For 18-micrometer-thick films of LC observed through an optical microscope (crossed polars), color encodes information about the azimuthal orientation of the LC with respect to the two orthogonal polarizers and the zenithal angle of the LCs with respect to the axis normal to the plane of the film<sup>1</sup>. Thus, spatio-temporal color patterns encode information regarding the transition of LCs from homeotropic to planar anchoring (i.e., interference colors). When analyzed using the A\* channel, a continuous anchoring transition of LC will exhibit oscillations between negative (green) and positive (red) values of A\* (as shown in Figure 7a). In Figure 7, we present experimental characterization of anchoring transitions of LC triggered by exposure to either pure Cl<sub>2</sub> (5ppm), pure O<sub>3</sub> (5ppm), or a mixture (5ppm Cl<sub>2</sub> and 5ppm O<sub>3</sub>). Inspection of the results

for the two pure gases reveals two observations. First, the LC response to pure  $Cl_2$  exhibits no oscillation in  $A^*$  (Figure 7b), consistent with the earlier observation that  $Cl_2$  triggers a discontinuous anchoring transition on  $Mn(ClO_4)_2$  surfaces in Figure 1a. Second, in contrast to  $Cl_2$ , the response to pure  $O_3$  leads to high amplitude oscillations in  $A^*$  (Figure 7c), also consistent with experimental observations in Figure 1 indicating a continuous change in tilt of the LC during the response to  $O_3$ . The limited information encoded in the color dynamics of pure  $Cl_2$  provides further insight into why it is more difficult to detect this analyte (compared to  $O_3$ , for which color dynamics provide richer information).

In comparison to pure gases, the response of the LC to the mixture of  $\text{Cl}_2$  and  $\text{O}_3$  reveals oscillations in A\* (Figure 7d), but the oscillations are lower in amplitude than those of pure  $\text{O}_3$ . From the A\* field plotted below the spatially averaged A\* values, we also see that, in the presence of a gaseous mixture, the LC response involves the formation of multiple domains (each exhibiting a continuous LC anchoring transitions; at a

given instant in time, some domains are red and some are green). These individual domains begin their reorientation at different times and reorient at different rates. This results in weak fluctuations in  $A^*$ , as the fluctuations are dampened during the spatial averaging. The nature of this response contrasts to that of pure  $O_3$ , where there is a single connected domain that oscillates at a single frequency and this translates to high fluctuations in  $A^*$ .

Finally, observations of the A\* response during  $Cl_2$  detection in mixtures with  $O_3$  reveal that color fluctuations appear sooner (50 sec, Figure 7d) than the optical response of the LC to pure  $Cl_2$  (300 sec, Figure 7b). This indicates that the presence of  $O_3$  in the mixture accelerates the LC response to  $Cl_2$ ; in other words, the analytes have a synergistic effect. This apparent synergy is confirmed by our observation that LCNet enables detection of  $Cl_2$  with concentrations that are as low as 1 ppm in mixtures that are dominated by  $O_3$  (concentrations of 650 ppm). Additional studies aimed at understanding the origin of this synergy are ongoing and will be reported elsewhere.

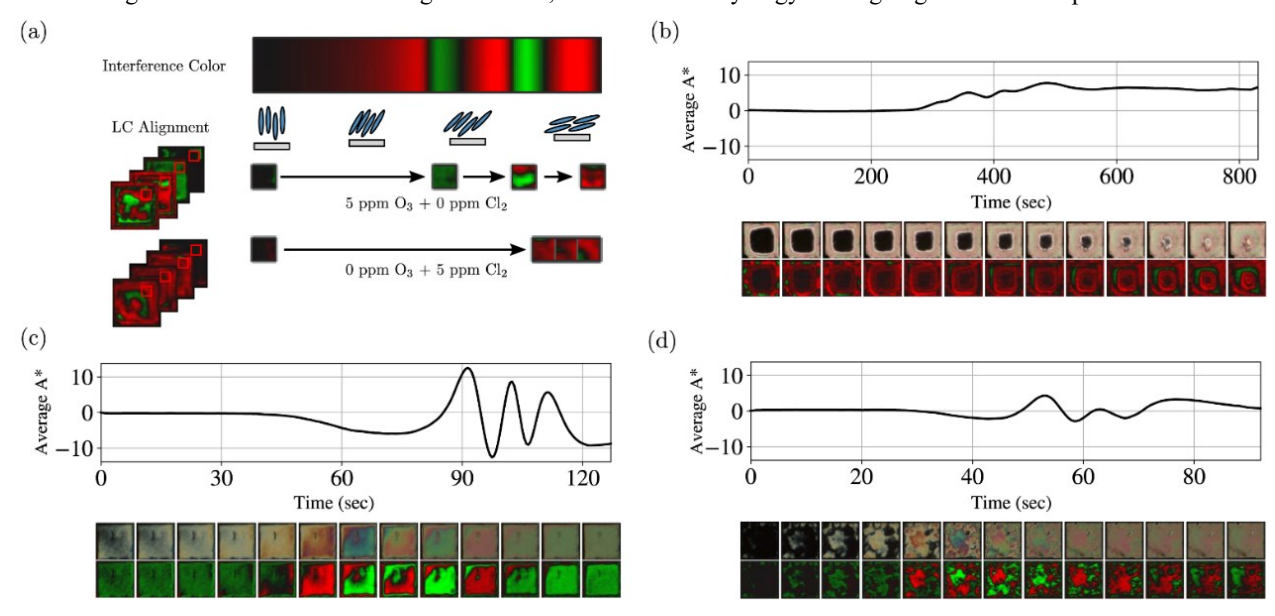


**Figure 7.** (a) Visualization of interference colors in A\* created by white light illumination when liquid crystals transition from homeotropic to planar. The red-green transformation cycles several times. Pure O<sub>3</sub> triggers a *continuous* anchoring transition, resulting in a continuous evolution of interference colors in A\*. Pure Cl<sub>2</sub> triggers a *discontinuous* anchoring transition, resulting in a "jump" in interference colors in A\*. (b)-(d) Spatial-average of A\* for pure 5 ppm Cl<sub>2</sub>, pure 5 ppm O<sub>3</sub>, and a mixture of 5 ppm O<sub>3</sub> + 5ppm Cl<sub>2</sub> and A\* channels. The time ranges for selected snapshots are from 400 to 700 seconds, 63 to 125 seconds, and 60 to 91 seconds, respectively. These time ranges capture the A\* signal during the response. (b) Exposure to 5ppm Cl<sub>2</sub> results in a discontinuous LC transition and thus no oscillations in the average A\* value. (c) Exposure to 5ppm O<sub>3</sub> induces the formation of a single domain that has a continuous LC transition that represents a large amplitude oscillation in the spatially averaged A\*. (d) Exposure to 5ppm Cl<sub>2</sub> + 5ppm O<sub>3</sub> mixture forms multiple domains in the LC film that reorient continuously. These domains begin the transition at different times and different speeds, causing the oscillations of A\* to be of lower amplitude than those found in the response to pure O<sub>3</sub>.

## CONCLUSIONS

We report experimental measurements of the optical responses of LC films supported on  $Mn(ClO_4)_2$ -decorated surfaces to mixtures of  $O_3$  and  $Cl_2$ , and we use the experimental datasets to train a 3D CNN architecture (called LCNet) to extract spatial, temporal, and color information from the optical responses of the LC films to the gas mixtures. We show that this information enables the detection of each species of gas within the mixture as well as prediction of their concentrations at levels relevant to the targeted contaminants. We also show we can detect the presence of  $Cl_2$  even when the concentration of  $O_3$  is orders of magnitude greater than the  $Cl_2$  concentration. The proposed methodology has attributes (low cost, small monitoring device) that have the potential to greatly improve personal exposure measurements of air pollutants in industrial

and urban contexts to support human health studies. The simultaneous monitoring of ozone and chlorine gas are used as examples of a criteria pollutant and hazardous air pollutants (HAP), respectively, thus showing that the integration of LC and 3D CNN can allow the simultaneous monitoring of both classes of air pollutants.

We use simplified data representations, saliency analysis, and color analysis to identify main features of the LC response that enable simultaneous detection of O<sub>3</sub> and Cl<sub>2</sub>. This analysis reveals that O<sub>3</sub> detection is driven by the transition time over which the brightness of the LC changes, while Cl<sub>2</sub> detection is driven by color fluctuations that develop late in the optical response of the LC. Our analysis also reveals that a color field called A\* provides a reliable descriptor for analysis of the color dynamics of the LC response (e.g., enables detection of

continuous/discontinuous anchoring transitions of LC). Our approach to capturing spatiotemporal color patterns of the LC in a thin film geometry is generalizable and is applicable to analysis of LC responses in other geometries (e.g., fiber  $^{19,23}$  and droplet  $^{41}$ ). Our study also identifies synergistic effects of the two gases on the LC response, synergy that permits detection of Cl2 in the mixture more rapidly than in pure Cl2 gas. Future studies will use density functional theory and molecular dynamics simulations to understand synergistic effects that arise in gaseous mixtures and to study how changes in the design can improve sensor performance.

In this paper, we focus on the development of a machine learning methodology for analysis of Cl<sub>2</sub> and O<sub>3</sub> using gas mixtures with concentrations in the ppm range. However, the LC-based approach reported here has the potential to be extended to detection of mixtures of Cl<sub>2</sub> and O<sub>3</sub> in the parts-per-billion (ppb) range. For example, previously we demonstrated detection of 200 ppb of Cl<sub>2</sub> (as a single gas component).<sup>28</sup> Additionally, we have performed preliminary measurements demonstrating detection of 220 ppb of O<sub>3</sub> (see details in SI; Section S9). We envisage future directions of investigation that extend the methodology reported in this paper to the analysis of gas mixtures in the ppb concentration range.

#### ASSOCIATED CONTENT

**Supporting Information**. Additional details regarding experimental methods and machine learning methodology. This material is available free of charge via the Internet at http://pubs.acs.org."

#### **AUTHOR INFORMATION**

#### Corresponding Author

- \* victor.zavala@wisc.edu (Victor M. Zavala)
- \* nla34@cornell.edu (Nicholas L. Abbott)

#### **Author Contributions**

‡N.B., S.J., and A.S. contributed equally to this work.

#### Notes

N.L.A. declares a financial interest in Platypus Technologies LLC, a for-profit company that has developed LC-based analytic technologies.

## **ACKNOWLEDGMENT**

We acknowledge financial support from the US National Science Foundation under grants IIS-1837812 and 1837821. This work was also partially supported by the Cornell Center for Materials Research with funding from the NSF MRSEC program (DMR-1719875).

#### **REFERENCES**

- (1) Karanikas, N.; Foster, C.; Beltran Hernandez, A.; Harvey, A.; Targal, O.; Horswill, N. Conventional and Alternative Aviation Fuels: Occupational Exposure and Health Effects. ACS Chem. Heal. Saf. 2021, 28 (3), 159–170.
- (2) Ashley, K. Developments in Electrochemical Sensors for Occupational and Environmental Health Applications. J. Hazard. Mater. 2003, 102 (1), 1–12.
- (3) Chen, L.; Wu, D.; Yoon, J. Recent Advances in the Development of Chromophore-Based Chemosensors for Nerve Agents and Phosgene. ACS Sensors 2018, 3 (1), 27–43.
- (4) Davidson, C. E.; Dixon, M. M.; Williams, B. R.; Kilper, G. K.;

- Lim, S. H.; Martino, R. A.; Rhodes, P.; Hulet, M. S.; Miles, R. W.; Samuels, A. C.; Emanuel, P. A.; Miklos, A. E. Detection of Chemical Warfare Agents by Colorimetric Sensor Arrays. *ACS Sensors* **2020**, *5* (4), 1102–1109.
- (5) Righettoni, M.; Tricoli, A.; Pratsinis, S. E. Si:WO<sub>3</sub> Sensors for Highly Selective Detection of Acetone for Easy Diagnosis of Diabetes by Breath Analysis. *Anal. Chem.* 2010, 82 (9), 3581– 3587
- (6) Liu, Y.; Pharr, M.; Salvatore, G. A. Lab-on-Skin: A Review of Flexible and Stretchable Electronics for Wearable Health Monitoring. ACS Nano 2017, 11 (10), 9614–9635.
- (7) Teymourian, H.; Parrilla, M.; Sempionatto, J. R.; Montiel, N. F.; Barfidokht, A.; Van Echelpoel, R.; De Wael, K.; Wang, J. Wearable Electrochemical Sensors for the Monitoring and Screening of Drugs. ACS Sensors 2020, 5 (9), 2679–2700.
- (8) Klemas, V. V. Coastal and Environmental Remote Sensing from Unmanned Aerial Vehicles: An Overview. J. Coast. Res. 2015, 31, 1260–1267.
- (9) Schierenbeck, T. M.; Smith, M. C. Path to Impact for Autonomous Field Deployable Chemical Sensors: A Case Study of in Situ Nitrite Sensors. *Environ. Sci. Technol.* 2017, 51 (9), 4755–4771.
- (10) Sui, N.; Zhang, P.; Zhou, T.; Zhang, T. Selective Ppb-Level Ozone Gas Sensor Based on Hierarchical Branch-like In<sub>2</sub>O<sub>3</sub> Nanostructure. Sensors Actuators B Chem. 2021, 336, 129612.
- (11) Lo, T.-H.; Shih, P.-Y.; Wu, C.-H. The Response of UV/Blue Light and Ozone Sensing Using Ag-TiO<sub>2</sub> Planar Nanocomposite Thin Film. Sensors 2019, 19 (23), 5061.
- (12) Avansi, W.; Catto, A. C.; da Silva, L. F.; Fiorido, T.; Bernardini, S.; Mastelaro, V. R.; Aguir, K.; Arenal, R. One-Dimensional V<sub>2</sub>O<sub>5</sub>/TiO<sub>2</sub> Heterostructures for Chemiresistive Ozone Sensors. ACS Appl. Nano Mater. 2019, 2 (8), 4756–4764.
- (13) Wu, C.-H.; Chang, K.-W.; Li, Y.-N.; Deng, Z.-Y.; Chen, K.-L.; Jeng, C.-C.; Wu, R.-J.; Chen, J.-H. Improving the Sensitive and Selective of Trace Amount Ozone Sensor on Indium-Gallium-Zinc Oxide Thin Film by Ultraviolet Irradiation. Sensors Actuators B Chem. 2018, 273, 1713–1718.
- (14) Baron, R.; Saffell, J. Amperometric Gas Sensors as a Low Cost Emerging Technology Platform for Air Quality Monitoring Applications: A Review. ACS Sensors 2017, 2 (11), 1553–1566.
- (15) Hossain, M.; Saffell, J.; Baron, R. Differentiating NO<sub>2</sub> and O<sub>3</sub> at Low Cost Air Quality Amperometric Gas Sensors. ACS Sensors 2016, 1 (11), 1291–1294.
- (16) Petruci, J. F. da S.; Barreto, D. N.; Dias, M. A.; Felix, E. P.; Cardoso, A. A. Analytical Methods Applied for Ozone Gas Detection: A Review. *TrAC Trends Anal. Chem.* 2022, 149, 116552.
- (17) Robinson, S. E.; Grinwald, B. A.; Bremer, L. L.; Kupcho, K. A.; Acharya, B. R.; Owens, P. D. A Liquid Crystal-Based Passive Badge for Personal Monitoring of Exposure to Hydrogen Sulfide. J. Occup. Environ. Hyg. 2014, 11 (11), 741–750.
- (18) Xu, Y.; Rather, A. M.; Song, S.; Fang, J.-C.; Dupont, R. L.; Kara, U. I.; Chang, Y.; Paulson, J. A.; Qin, R.; Bao, X.; Wang, X. Ultrasensitive and Selective Detection of SARS-CoV-2 Using Thermotropic Liquid Crystals and Image-Based Machine Learning. Cell Reports Phys. Sci. 2020, 1 (12), 100276.
- (19) Schelski, K.; Reyes, C. G.; Pschyklenk, L.; Kaul, P.-M.; Lagerwall, J. P. F. Quantitative Volatile Organic Compound Sensing with Liquid Crystal Core Fibers. *Cell Reports Phys. Sci.* 2021, 100661.
- (20) Spengler, M.; Pschyklenk, L.; Niemeyer, J.; Kaul, P.; Giese, M. Photonic NO<sub>2</sub> Gas Sensing with Binaphthyl-Based Dopants. Adv. Opt. Mater. 2021, 9 (7), 2001828.
- (21) Pschyklenk, L.; Wagner, T.; Lorenz, A.; Kaul, P. Optical Gas Sensing with Encapsulated Chiral-Nematic Liquid Crystals. ACS Appl. Polym. Mater. 2020, 2 (5), 1925–1932.
- (22) Shibaev, P. V.; Carrozzi, D.; Vigilia, L.; DeWeese, H. Liquid Crystal Nose, Chiral Case: Towards Increased Selectivity and Low Detection Limits. *Liq. Cryst.* 2019, 46 (9), 1309–1317.
- (23) Reyes, C. G.; Sharma, A.; Lagerwall, J. P. F. Non-Electronic Gas Sensors from Electrospun Mats of Liquid Crystal Core Fibres for Detecting Volatile Organic Compounds at Room Temperature.

- Liq. Cryst. 2016, 43 (13-15), 1986-2001.
- (24) Han, Y.; Pacheco, K.; Bastiaansen, C. W. M.; Broer, D. J.; Sijbesma, R. P. Optical Monitoring of Gases with Cholesteric Liquid Crystals. J. Am. Chem. Soc. 2010, 132 (9), 2961–2967.
- (25) Mujahid, A.; Stathopulos, H.; Lieberzeit, P. A.; Dickert, F. L. Solvent Vapour Detection with Cholesteric Liquid Crystals—Optical and Mass-Sensitive Evaluation of the Sensor Mechanism. Sensors 2010, 10 (5), 4887–4897.
- (26) Yokoyama, H. Surface Anchoring of Nematic Liquid Crystals. Mol. Cryst. Liq. Cryst. Inc. Nonlinear Opt. 1988, 165, 265–361.
- (27) Jerome, B. Surface Effects and Anchoring in Liquid Crystals. Reports Prog. Phys. 1991, 54, 391–451.
- (28) Brake, J. M.; Daschner, M. K.; Luk, Y. Y.; Abbott, N. L. Biomolecular Interactions at Phospholipid-Decorated Surfaces of Liquid Crystals. *Science* (80-.). 2003, 302, 2094–2097.
- (29) Woltman, S. J.; Jay, G. D.; Crawford, G. P. Liquid-Crystal Materials Find a New Order in Biomedical Applications. *Nat. Mater.* 2007, 6, 929–938.
- (30) Bi, X.; Hartono, D.; Yang, K. L. Real-Time Liquid Crystal PH Sensor for Monitoring Enzymatic Activities of Penicillinase. Adv. Funct. Mater. 2009, 19 (23), 3760–3765.
- (31) Nayani, K.; Rai, P.; Bao, N.; Yu, H.; Mavrikakis, M.; Twieg, R. J.; Abbott, N. L. Liquid Crystals with Interfacial Ordering That Enhances Responsiveness to Chemical Targets. *Adv. Mater.* 2018, 30 (27), 1706707.
- (32) Shah, R. R.; Abbott, N. L. Principles for Measurement of Chemical Exposure Based on Recognition-Driven Anchoring Transitions in Liquid Crystals. Science (80-.). 2001, 293 (5533), 1296–1299.
- (33) Szilvási, T.; Yu, H.; Gold, J. I.; Bao, N.; Wolter, T. J.; Twieg, R. J.; Abbott, N. L.; Mavrikakis, M. Coupling the Chemical Reactivity of Bimetallic Surfaces to the Orientations of Liquid Crystals. *Mater. Horizons* 2021, 8 (7), 2050–2056.
- (34) Szilvási, T.; Bao, N.; Yu, H.; Twieg, R. J.; Mavrikakis, M.; Abbott, N. L. The Role of Anions in Adsorbate-Induced Anchoring Transitions of Liquid Crystals on Surfaces with Discrete Cation Binding Sites. Soft Matter 2018, 14 (5), 797– 805
- (35) Yu, H.; Szilvási, T.; Wang, K.; Gold, J. I.; Bao, N.; Twieg, R. J.; Mavrikakis, M.; Abbott, N. L. Amplification of Elementary Surface Reaction Steps on Transition Metal Surfaces Using Liquid Crystals: Dissociative Adsorption and Dehydrogenation. J. Am. Chem. Soc. 2019, 141 (40), 16003–16013.
- (36) Lambert, A.; Valiulis, S.; Cheng, Q. Advances in Optical Sensing and Bioanalysis Enabled by 3D Printing. ACS Sensors 2018, 3 (12), 2475–2491.
- (37) Collivignarelli, M. C.; Abbà, A.; Benigna, I.; Sorlini, S.; Torretta, V. Overview of the Main Disinfection Processes for Wastewater and Drinking Water Treatment Plants. Sustain. 2018, 10, 86.
- (38) Di, Q.; Wang, Y.; Zanobetti, A.; Wang, Y.; Koutrakis, P.; Choirat, C.; Dominici, F.; Schwartz, J. D. Air Pollution and Mortality in the Medicare Population. N. Engl. J. Med. 2017, 376 (26), 2513–2522.
- (39) Cao, Y.; Yu, H.; Abbott, N. L.; Zavala, V. M. Machine Learning Algorithms for Liquid Crystal-Based Sensors. ACS Sensors 2018, 3 (11), 2237–2245.

- (40) Smith, A.; Abbott, N.; Zavala, V. M. Convolutional Network Analysis of Optical Micrographs for Liquid Crystal Sensors. J. Phys. Chem. C 2020, 124 (28), 15152.
- (41) Frazão, J.; Palma, S. I. C. J.; Costa, H. M. A.; Alves, C.; Roque, A. C. A.; Silveira, M. Optical Gas Sensing with Liquid Crystal Droplets and Convolutional Neural Networks. Sensors 2021, 21 (8), 2854.
- (42) Simonyan, K.; Vedaldi, A.; Zisserman, A. Deep inside Convolutional Networks: Visualising Image Classification Models and Saliency Maps. In 2nd International Conference on Learning Representations, ICLR 2014 - Workshop Track Proceedings; 2014.
- (43) Rakness, K.; Gordon, G.; Langlais, B.; Masschelein, W.; Matsumoto, N.; Richard, Y.; Robson, C. M.; Somiya, I. Guideline for Measurement of Ozone Concentration in the Process Gas from an Ozone Generator. *Ozone Sci. Eng.* 1996, 18 (3), 209–229.
- (44) Triandi Tjahjanto, R.; Galuh R., D.; Wardhani, S. Ozone Determination: A Comparison of Quantitative Analysis Methods. J. Pure Appl. Chem. Res. 2012, 1 (1), 18–25.
- (45) Hunter, J. T.; Abbott, N. L. Dynamics of the Chemo-Optical Response of Supported Films of Nematic Liquid Crystals. Sensors Actuators, B Chem. 2013, 183, 71–80.
- (46) Stumpel, J. E.; Wouters, C.; Herzer, N.; Ziegler, J.; Broer, D. J.; Bastiaansen, C. W. M.; Schenning, A. P. H. J. An Optical Sensor for Volatile Amines Based on an Inkjet-Printed, Hydrogen-Bonded, Cholesteric Liquid Crystalline Film. Adv. Opt. Mater. 2014, 2 (5), 459–464.
- (47) Wang, J.; Jákli, A.; West, J. L. Liquid Crystal/Polymer Fiber Mats as Sensitive Chemical Sensors. J. Mol. Liq. 2018, 267 (1), 490–495.
- (48) Abadi, M.; Barham, P.; Chen, J.; Chen, Z.; Davis, A.; Dean, J.; Devin, M.; Ghemawat, S.; Irving, G.; Isard, M.; Kudlur, M.; Levenberg, J.; Monga, R.; Moore, S.; Murray, D. G.; Steiner, B.; Tucker, P.; Vasudevan, V.; Warden, P.; Wicke, M.; Yu, Y.; Zheng, X. TensorFlow: A System for Large-Scale Machine Learning. In *Proceedings of the 12th USENIX Symposium on Operating Systems Design and Implementation, OSDI 2016*; 2016; pp 265–283.
- (49) Hastie, T.; Tibshirani, R.; Friedman, J. The Elements of Statistical Learning; Springer Science & Business Media, 2009.
- (50) Berrar, D. Cross-Validation. In Encyclopedia of Bioinformatics and Computational Biology; Elsevier, 2019; pp 542–545.
- (51) Szilvási, T.; Bao, N.; Nayani, K.; Yu, H.; Rai, P.; Twieg, R. J.; Mavrikakis, M.; Abbott, N. L. Redox-Triggered Orientational Responses of Liquid Crystals to Chlorine Gas. *Angew. Chemie Int. Ed.* 2018, 57 (31), 9665–9669.
- (52) Bao, N.; Gold, J. I.; Szilvási, T.; Yu, H.; Twieg, R. J.; Mavrikakis, M.; Abbott, N. L. Designing Chemically Selective Liquid Crystalline Materials That Respond to Oxidizing Gases. J. Mater. Chem. C 2021, 9 (20), 6507–6517.
- (53) Nieuwenhuizen, M. S.; Harteveld, J. L. N. Studies on a Surface Acoustic Wave (SAW) Dosimeter Sensor for Organophosphorous Nerve Agents. Sensors Actuators B Chem. 1997, 40 (2–3), 167–173.
- (54) Paschos, G. Perceptually Uniform Color Spaces for Color Texture Analysis: An Empirical Evaluation. *IEEE Trans. Image* Process. 2001, 10 (6), 932–937.

## Table of Contents artwork

